

Influence of disorder on a Bragg microcavity

S. G. TIKHODEEV,^{1,2,*} E. A. MULJAROV,³ W. LANGBEIN,³ N. A. GIPPIUS,⁴ H. GIESSEN,⁵ AND T. WEISS,⁵

¹*M. V. Lomonosov Moscow State University, Leninskie Gory 1, Moscow 119991, Russia*

²*A. M. Prokhorov General Physics Institute, Russian Academy of Sciences, Vavilova Street 38, Moscow 119991, Russia*

³*Cardiff University, School of Physics and Astronomy, The Parade, CF24 3AA, Cardiff, United Kingdom*

⁴*Skolkovo Institute of Science and Technology, Nobel Street 3, Moscow 143025, Russia*

⁵*4th Physics Institute and Research Center SCoPE, University of Stuttgart, Stuttgart D-70550, Germany*

**tikh@gpi.ru*

<https://doi.org/10.1364/JOSAB.402986>.

Journal of the Optical Society of America B, Vol. 38, No. 1, pp. 139–150 (2021)

Abstract: Using the resonant-state expansion for leaky optical modes of a planar Bragg microcavity, we investigate the influence of disorder on its fundamental cavity mode. We model the disorder by randomly varying the thickness of the Bragg-pair slabs (composing the mirrors) and the cavity, and calculate the resonant energy and linewidth of each disordered microcavity exactly, comparing the results with the resonant-state expansion for a large basis set and within its first and second orders of perturbation theory. We show that random shifts of interfaces cause a growth of the inhomogeneous broadening of the fundamental mode that is proportional to the magnitude of disorder. Simultaneously, the quality factor of the microcavity decreases inversely proportional to the square of the magnitude of disorder. We also find that first-order perturbation theory works very accurately up to a reasonably large disorder magnitude, especially for calculating the resonance energy, which allows us to derive qualitatively the scaling of the microcavity properties with disorder strength.

© 2021 Optical Society of America

1. Introduction

Disorder plays an important role in photonics. For example, it drives the coloring and polarization conversion of natural disordered light diffusers such as opals, birds feathers, or wings of butterflies [1–5]. Unavoidable technological imperfections can sometimes critically reduce the desired performance of photonic crystal slab waveguides and nanocavities [6–9]. Different theoretical approaches have been proposed to describe the role of disorder, either numerically [10, 11] or based on various versions of perturbation theory in electrodynamics [6, 12–15]. The important prerequisite for any perturbation theory is a suitable basis, which, in the case of open electrodynamical systems, is composed of resonant states (also known as quasi-normal or leaky modes) [16–27] that determine the resonant optical response, e.g., the Fano resonances in open cavities [28–30].

Recently, the resonant-state expansion, a rigorous perturbation theory for calculating the resonant states of any open system in electrodynamics based on a finite number of resonant states of some more elementary system, has been developed [19]. Originally proposed for purely dielectric shapes (slabs, microspheres, microcavities [20]) with nondispersive dielectric permittivity, the method was then generalized to dispersive open systems [31], photonic crystal slabs [32], and periodic arrays of nanoantennas at normal [33] and oblique incidence [34], and open systems containing magnetic, chiral, or bi-anisotropic materials [35]. In addition, the method has been extended to waveguide geometries such as dielectric slab waveguides [36, 37] and optical fibers [38], with a possibility to account for nonuniformities [39] and nonlinearities [40, 41].

The perturbation in the resonant-state expansion can be of any shape within the basis volume.

The difference from the basis reference can even be huge when using a sufficiently large number of resonant states as basis. In order to have a meaningful physical picture, it is, however, better to describe the structure of interest using a minimum number of resonant states, see, e.g., examples of calculating the sensor performance with a single resonant state first-order approximation [33, 42], and the interaction of spatially separated photonic crystal slabs with a pair of quasi-degenerate states in Ref. [34].

While full-wave simulations have been already used to investigate the resonant states in disordered media [25], we concentrate in this paper on the impact of disorder on the resonant states of a Bragg microcavity by comparing full-wave calculations with the resonant-state expansion as well as its first- and second-order perturbative formulations. In particular, we vary randomly the thickness of the Bragg-pair slabs (acting as the mirrors) and the cavity itself, and derive how the resonant states change with growing amplitude of random displacements. On the one hand, because of the simplicity of the system, its disorder-modified states (their energies, linewidths, and field distributions) can be calculated with any accuracy via linearization of the frequency dependence of the inverse scattering matrix around the resonant state of interest [18, 43, 44] for each disorder realization. On the other hand, we can calculate the same resonances using the resonant-state expansion for an increasing number of resonant states in the basis, and then compare them with the exact values. Repeating the calculations many times and retrieving the statistically averaged results yields relevant information about the influence of disorder on the optical properties of the Bragg microcavities. A similar approach has been used in Ref. [38] where the impact of disorder on the effective index of propagating modes in photonic crystal fibers has been investigated via the resonant-state expansion and compared with full-wave simulations.

The paper is organized as follows: The model of the disordered Bragg microcavity is described in Sec. 2, the formulation of the resonant-state expansion is given in Sec. 3. Section 4 summarizes the results of the comparison between the exact solutions and those obtained by the resonant-state expansion using different orders of perturbation theory. Special attention is paid to the disorder-induced inhomogeneous broadening in the ensemble of disordered cavities (Subsec. 4.1) and the analysis of the influence of disorder magnitude on the statistically averaged resonance energies and their homogeneous linewidths (Subsec. 4.2). Section 5 contains a discussion of the obtained results, which are summarized in Sec. 6. Details of the linearization scheme of calculating the poles of the scattering matrix are given in Appendix A. The accuracy of the different orders of perturbation theory based on the resonant-state expansion, depending on the magnitude of disorder is discussed in Appendix B.

2. Model

We consider a planar microcavity that is made of two Bragg mirrors with m pairs of layers of $\lambda/4$ optical thickness of nondispersive materials with dielectric constants ε_1 and ε_2 , surrounding a cavity layer of $M \times \lambda/2$ optical thickness of material with dielectric constant ε_1 . The cavity is surrounded by free space with permittivity $\varepsilon_0 = 1$. In the numerical results presented we use $\varepsilon_1 = 10$, $\varepsilon_2 = 4$, $m = 4$, and $M = 2$, the latter corresponding to a cavity layer of λ optical thickness. A schematic of the microcavity is displayed in Fig. 1. We have chosen the parameters of the cavity such that the fundamental cavity mode at normal incidence is $\Omega_0 = 2\pi\hbar c/\lambda = 1$ eV ($\lambda = 1.24$ μm). This corresponds to thicknesses of the Bragg $\lambda/4$ layers of $L_1 = \pi c\hbar/(2\sqrt{\varepsilon_1}\Omega_0) \approx 98$ nm and $L_2 = \pi c\hbar/(2\sqrt{\varepsilon_2}\Omega_0) \approx 155$ nm, and the central cavity layer is $L_C = 4L_1 \approx 392$ nm thick. Then the fundamental cavity mode linewidth appears to be $2\Gamma_0 = 2.8$ meV corresponding to the quality factor $Q = \Omega_0/2\Gamma_0 \approx 356$. The spatial distributions $\text{Re } \mathcal{E}_0$ and $\text{Im } \mathcal{E}_0$ of the resonant electric field of the fundamental cavity mode with eigenenergy $E_0 = \Omega_0 - i\Gamma_0$ are shown in Fig. 1 by blue and red curves, respectively.

The optical scattering matrix of this simple microcavity (see in Appendix A) has an infinite

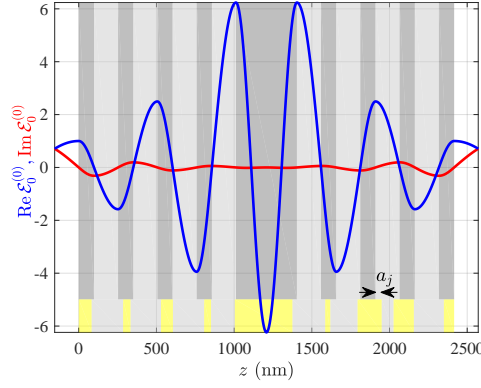


Fig. 1. (Color online) Schematic of the unperturbed Bragg microcavity (gray background) and spatial distributions of the real (blue solid line) and imaginary (red solid line) parts of the electric field $\mathcal{E}_0^{(0)}(z)$ of the fundamental cavity mode. Darker and brighter gray shades indicate materials with dielectric susceptibilities $\varepsilon_1 = 10$ and $\varepsilon_2 = 4$, respectively. Yellow/bright gray shades illustrate a realization of a microcavity with interfaces randomly displaced by shifts a_j , with disorder strength $a = 0.5$ [see Eq. (1)]

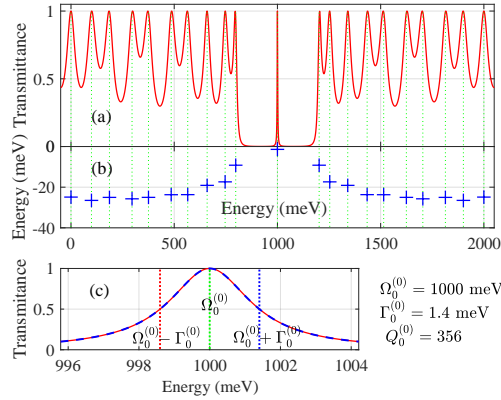


Fig. 2. (Color online) (a) Transmittance of the ideal microcavity as depicted in Fig. 1 (without random displacements). (b) Map of resonant states of the microcavity on the complex energy plane (crosses); the vertical green dashed lines denote the positions of the resonant states on the real energy axis. (c) Transmission spectra in the vicinity of the fundamental resonance at 1 eV (red curve). The dashed blue curve shows the single-pole resonant approximation given by Eq. (17). Green, red, and blue vertical dashed lines mark the energies Ω_0 , $\Omega_0 - \Gamma_0$, and $\Omega_0 + \Gamma_0$, respectively.

series of discrete Fabry-Perot poles on the complex energy plane, which manifest themselves as peaks in the transmission spectrum, as shown in Figs. 2a,b.

The transmission spectrum in Fig. 2 has been calculated within a 2×2 optical scattering matrix approach as described in Ref. [17] for homogeneous layers and normally incident light. More details are provided in Appendix A. The poles of the scattering matrix on the complex energy plane in Fig. 2b, as well as the electric eigenfields in Fig. 1 can be calculated via the scattering matrix energy dispersion linearization [18, 43, 44], as described in Appendix A.

The real part of the eigenenergy, $\Omega_n = \text{Re } E_n$, corresponds to the resonance energy, while the imaginary part, $2\Gamma_n = -2\text{Im } E_n$, gives the resonance linewidth. In what follows, we mark the values corresponding to the unperturbed (ideal) microcavity by the upper index (0), as shown in Figs. 1,2.

We now investigate the behavior of the fundamental cavity mode denoted by eigenenergy E_0 under the influence of random displacements of the microcavity interfaces. We will leave the external interfaces of the microcavity at their original positions, and assume that all other $j = 1, 2, \dots, J$ ($J = 16$) interfaces are shifted by

$$a_j = a\beta_j L_1, \quad (1)$$

where $\beta_1, \beta_2, \dots, \beta_J$ is a set of J uniformly distributed uncorrelated random numbers within the interval $(-1, 1)$. The disorder strength a is chosen between zero and 0.5 in order to keep all resulting layer thicknesses positive. Furthermore, we consider uncorrelated disorder with vanishing statistically averaged displacements

$$\langle \beta_j \rangle = 0. \quad (2)$$

Note that random shifts a_j of the interfaces have been measured experimentally before in disordered GaAs/AlAs cavities [45].

3. Resonant-state expansion

The resonant-state expansion [19, 20, 34, 46] relies on knowing the electric field distributions $\mathcal{E}_n^{(0)}(z)$ of a set of resonant states with complex frequencies $E_n^{(0)}$ for a photonic structure with a spatial profile of the dielectric susceptibility $\varepsilon^{(0)}(z)$. These resonant states are used in the resonant-state expansion as a basis to expand the electric fields of the resonant state of a modified structure with dielectric susceptibility

$$\varepsilon(z) = \varepsilon^{(0)}(z) + \Delta\varepsilon(z) \quad (3)$$

as

$$\mathcal{E}(z) = \sum_n b_n \frac{\mathcal{E}_n^{(0)}(z)}{C_n}. \quad (4)$$

The normalization constants C_n have the analytical form [19, 34]

$$C_n^2 = \int_0^L \varepsilon(z) \mathcal{E}_n^2(z) dz + \frac{i}{2k_n} [\mathcal{E}_n^2(0) + \mathcal{E}_n^2(L)], \quad (5)$$

where the range 0 to L covers exactly the microcavity structure, and the fields in the second term have to be taken in the medium outside the cavity. However, the fields are continuous at the outermost interfaces for the considered case of normal incidence, because this results in purely transverse electric fields over the entire microcavity. The general orthonormality of resonant states is given by [19, 34]

$$\begin{aligned} \delta_{n'n} = & \frac{1}{C_n C_n'} \left\{ \int_0^L \varepsilon(z) \mathcal{E}_{n'}(z) \mathcal{E}_n(z) dz \right. \\ & \left. + \frac{i}{k_{n'} + k_n} [\mathcal{E}_{n'}(0) \mathcal{E}_n(0) + \mathcal{E}_{n'}(L) \mathcal{E}_n(L)] \right\}, \end{aligned} \quad (6)$$

where $\hbar k_n = E_n/c$.

The coefficients b_n and new eigenenergies E can be calculated via the linear eigenproblem [19]

$$\sum_{n'} W_{nn'} b_{n'} = E b_n, \quad (7)$$

where

$$W_{nn'} = (A^{-1})_{nn'} E_n^{(0)}, \quad (8)$$

$$A_{nn'} = \delta_{nn'} + \frac{1}{2} V_{nn'}, \quad (9)$$

and the matrix elements of the perturbation are

$$V_{nn'} = \frac{1}{C_n C_{n'}} \int_0^L \Delta \varepsilon(z) \mathcal{E}_n^{(0)}(z) \mathcal{E}_{n'}^{(0)}(z) dz. \quad (10)$$

Following from the resonant-state expansion, the resonance eigenenergy in the first order of perturbation theory yields [34, 46]

$$E_n^{(1)} \approx E_n^{(0)} \left(1 + \frac{1}{2} V_{nn} \right)^{-1}, \quad (11)$$

whereas the resonant state eigenenergy up to the second order of perturbation theory is given by [46]

$$E_n^{(2)} \approx E_n^{(0)} \left(1 + \frac{1}{2} V_{nn} - \frac{1}{4} \sum_{n' \neq n} \frac{E_n^{(0)} V_{n'n}^2}{E_n^{(0)} - E_{n'}^{(0)}} \right)^{-1}. \quad (12)$$

In the following, we keep explicitly the normalization constants C_n in the resonant-state expansion formulas and use the eigenfields (e.g., the one shown in Fig. 1) satisfying the conditions

$$\mathcal{E}_n(0) = (-1)^{p_n} \mathcal{E}_n(L) = 1, \quad (13)$$

where $p_n = 0, 1$ denotes the eigenstate parity that is either even or odd due to the mirror symmetry of the unperturbed cavity. This choice of normalization is convenient for the calculation of the eigenfields within the linearization of the scattering matrix (see in Appendix A) and simplifies the comparison with the resonant-state expansion.

4. Influence of disorder

While investigating the influence of disorder, we compare the scattering matrix result from linearization, which we call here “exact”, with the first- and second-order approximations (11) and (12) as well as with the full resonant-state expansion obtained by solving the eigenvalue problem (7) with a truncation of an infinite matrix. The resonant-state expansion is asymptotically exact, and its only limitation is the basis size. The resonant states are calculated as described in Appendix A. The basis size is taken as $N = 419$ in the present paper, symmetrically around the fundamental cavity mode, see Appendix A. The same resonant states are used in the second-order perturbation theory.

Figure 3 illustrates changes of the real and imaginary parts of the fundamental cavity mode energy and linewidth for 1000 different realizations of random shifts of interfaces with the disorder parameter $a = 0.1505$. The latter means that the random displacements of the interfaces are up to ~ 15 nm.

It can be seen that (i) introducing disorder causes an inhomogeneous broadening of the resonance energy position, with a standard deviation on the order of 10 meV; (ii) the linewidth of the resonance (homogeneous broadening) grows by approximately 10% (from ~ 1.4 meV to

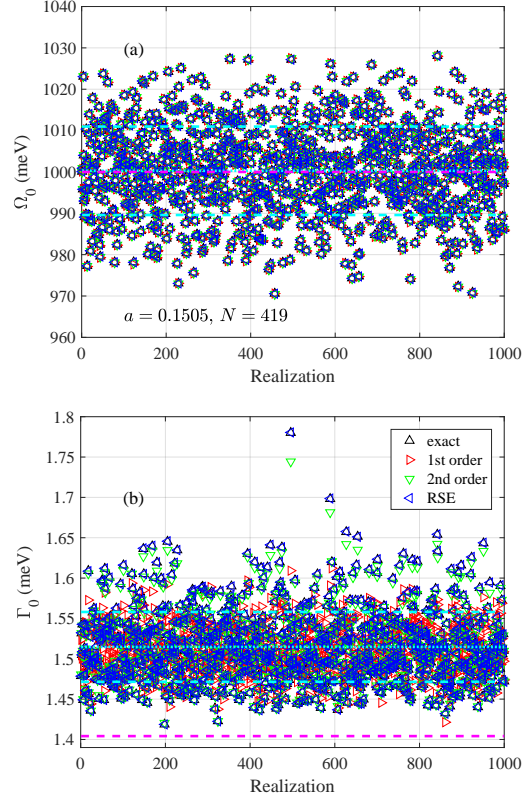


Fig. 3. (Color online) Example of calculated resonance frequencies Ω_0 (a) and half linewidths Γ_0 (b) of the fundamental microcavity resonance, for 1000 interface shift realizations with disorder parameter $a = 0.1505$. The legend in panel (b) specifies the symbols for the different results: Exact calculation, first- and second-order perturbation theory [Eq. (11) and (12), respectively], and resonant-state expansion (RSE) [Eq. (7)] with 419 basis states. Cyan dotted and dashed horizontal lines in panel (a) denote the mean values $\langle\Omega_0\rangle$ and $\langle\Omega_0\rangle \pm \sigma_\Omega$, where σ_Ω is the standard deviation of Ω_0 . The magenta dashed horizontal line indicates the resonance energy $\Omega_0^{(0)}$ of the unperturbed microcavity. Lines in panel (b) give the equivalent values for the resonance linewidth, i.e., $\langle\Gamma_0\rangle$, $\langle\Gamma_0\rangle \pm \sigma_\Gamma$, and $\Gamma_0^{(0)}$, where σ_Γ is the standard deviation of Γ_0 .

~ 1.52 meV); (iii) the results for the resonance energy Ω_0 (Fig. 3a), calculated exactly, in the first and second perturbation orders, and in the resonant-state expansion do visually coincide for all disorder realizations, while for the linewidth only the exact and the resonant-state expansion results coincide.

The difference, representing the calculation error between the exact results, the first, second and “full” resonant-state expansion (with $N = 419$ resonant states in the basis) is analyzed versus the disorder strength a in Appendix B. Since the absolute error is similar for the real and imaginary part, the relative error of calculating Ω_0 is approximately Q_0 times smaller than that of Γ_0 .

It is shown in Appendix B that the calculation error and its standard deviation grow with a and can be quite large, especially for the first perturbation order. Interestingly, the calculation errors for the quantities, averaged over many (1000 in this work) realizations, remain relatively small over the investigated range of disorder parameter $a \leq 0.3$, even in the first perturbation order.

In what follows we investigate the statistics of Ω_0 and Γ_0 as functions of the disorder parameter.

However, we begin from the analysis of the most visible effect of the disorder, namely the inhomogeneous broadening of the fundamental cavity mode eigenenergy distribution due to the disorder.

4.1. Inhomogeneous broadening

The distribution of fundamental cavity mode energies $\Omega_0(\nu)$ (where ν stands for the realization number of the random disorder) broadens with increasing disorder strength a , as is clearly seen in Fig. 3a (see also Appendix B). Physically, this would result in an inhomogeneous broadening of the transmission spectrum of a hypothetical large-area microcavity with randomly displaced inner interfaces, where the displacement changes gradually on some large-distance scale, and assuming incoherent addition of the transmission of different parts of this large microcavity. Such inhomogeneous broadening was observed, e.g., in high-quality factor III-V nitride microcavities [47] and attributed to homogeneous areas (at a local scale of $\sim 8 \mu\text{m}$), separated by fluctuations occurring on a short distance scale. The realization of high Q-factor in such microcavities is likely to be limited by the structural disorder [48, 49].

From comparison with Fig. 3b we see that for a disorder parameter $a = 0.1505$, the inhomogeneous broadening exceeds significantly the homogeneous linewidth, and it will be shown in the next section that the inhomogeneous broadening is equal to the homogeneous one for $a \approx 0.02$.

As to the distribution of resonance energies, as expected from the central limit theorem and the superposition of 16 independent uniformly distributed random variables β_j (see Eq. 1), it turns out to be close to normal Gaussian. A discretized density of states can be defined on an energy mesh with a small step $\delta < \Gamma_0$ as

$$P_\delta(E) = \frac{1}{\delta} \sum_{\nu} \int_{E-\delta/2}^{E+\delta/2} \delta(E' - \Omega_0(\nu)) dE', \quad (14)$$

where the sum is evaluated over all random realizations. It can be smoothed on a larger energy scale by convolution with a normalized rectangular function of width $\Delta \approx \Gamma_0$, resulting in the distribution

$$P_{\delta,\Delta}(E) = \frac{1}{\Delta} \int_{E-\Delta/2}^{E+\Delta/2} P_\delta(E') dE'. \quad (15)$$

Typical densities of states Eqs.(14) and (15) for the distribution of poles in Fig. 3a with an amplitude of disorder of $a = 0.1505$ are displayed as green and red lines in Fig. 4a for $\delta = 0.1 \text{ meV}$ and $\Delta = 1.5 \text{ meV}$. The averaged density is very close to the normal Gaussian distribution

$$P_{\text{Gauss}}(E) = \frac{1}{\sqrt{2\pi}\sigma_\Omega} \exp\left(-\frac{(E - \Omega_0^{(0)})^2}{2\sigma_\Omega^2}\right), \quad (16)$$

plotted as a blue dashed line in Fig. 4a, in accordance with the Central Limit Theorem. This theorem states that if you sum up a large number of random variables, the distribution of the sum will be approximately normal (i.e., Gaussian) under certain conditions, see, e.g., Ref. [50].

The transmission spectrum of the ideal microcavity in the vicinity of the fundamental cavity mode is approximated quite well by a Lorentzian

$$T(E, \Omega_0) = \frac{\Gamma_0^2}{(E - \Omega_0)^2 + \Gamma_0^2}, \quad (17)$$

see the solid and dashed lines in Fig. 2c. Thus, the inhomogeneously broadened spectrum of a large microcavity with the distribution of resonances is expected to exhibit the Voigt

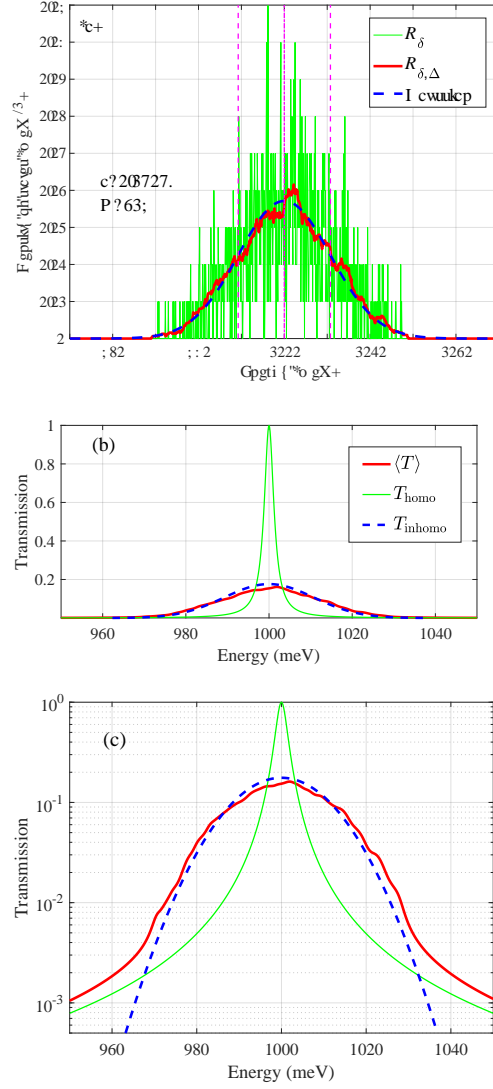


Fig. 4. (Color online) (a) Densities of states [Eqs. (14) and (15)], calculated with $\delta = 0.1$ meV and $\Delta = 1.5$ meV for the realizations of disorder in Fig. 3. Red vertical dashes denote $\Omega_0 \pm \sigma_\Omega$ and the solid line Ω_0 ; (b) Averaged inhomogeneously broadened transmission spectrum of a large cavity with all realizations of disorder (red solid curve). The green solid line is the homogeneously broadened transmission spectra of the ideal cavity calculated by Eq. (17). Blue dashed curves display Gaussian distributions [Eqs. (16) and (19)]; (c) same as panel (b) in logarithmic scale.

function [51, 52] shape,

$$\langle T(E) \rangle = \int T(E, \Omega_0) P_{\text{Gauss}}(\Omega_0) d\Omega_0. \quad (18)$$

In the limit $\Gamma_0 \ll \sigma_\Omega$ the averaged transmission is approximately Gaussian,

$$\langle T(E) \rangle \approx \frac{\Gamma_0}{\sigma_\Omega} \sqrt{\frac{\pi}{2}} \exp\left(-\frac{(E - \Omega_0^{(0)})^2}{2\sigma_\Omega^2}\right), \quad (19)$$

except for the Lorentzian tails for $|E - \Omega_0| > \sigma_\Omega$. An example of averaged spectra corresponding to the distribution of poles at disorder parameter $a = 0.1505$ for the convolution in Fig. 4a is given in Fig. 4b and in logarithmic scale in Fig. 4c. The averaged transmission spectra $\langle T(E) \rangle$ (red curves in panels b,c) coincide quite well with the Gaussian spectra, Eq. (19) (blue dashed curves) in the central part of the broadened resonance. In contrast, the Lorentzian tails approaching the homogeneously broadened spectrum Eq. (17) (solid green curves) are clearly visible in panel c due to the log scale.

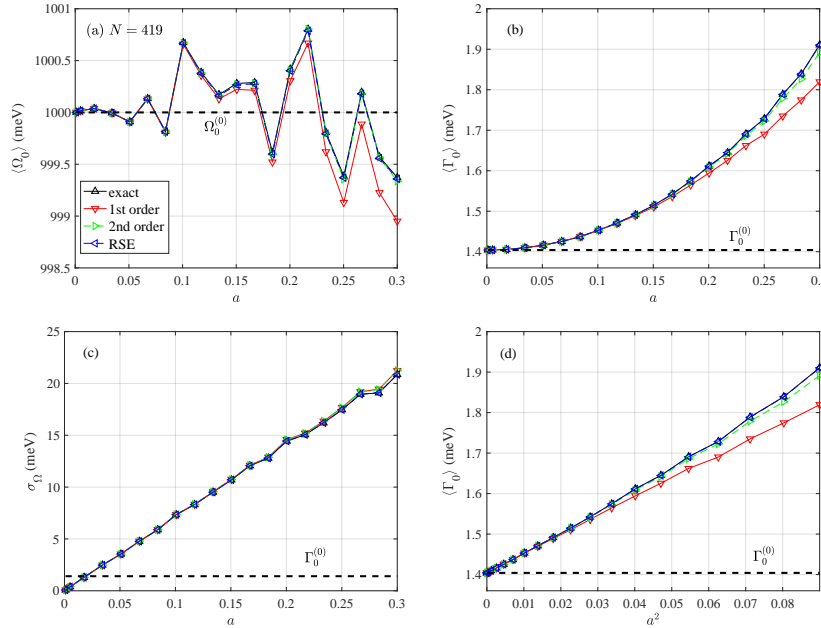


Fig. 5. (Color online) Resonance energy $\langle \Omega_0 \rangle$ (a) and half linewidth $\langle \Gamma_0 \rangle$ (b) as functions of disorder parameter a , averaged over 1000 realizations of random interface displacements. Panel (c) shows the standard deviation of resonance energy σ_Ω as a function of a , and panel (d) depicts $\langle \Gamma_0 \rangle$ as a function of a^2 . The values of $\Omega_0^{(0)}$ [$\Gamma_0^{(0)}$] for the ideal microcavity without disorder are shown as horizontal dashed lines in panel (a) [panels (b-d)].

4.2. Dependence on the disorder parameter

The dependence of the averaged parameters of the fundamental cavity mode on the disorder parameter a are illustrated in Fig. 5. Panels a and b display the averaged fundamental cavity mode energy $\langle \Omega_0 \rangle$ and half linewidth $\langle \Gamma_0 \rangle$, respectively, as functions of the disorder parameter a . The averaging is carried out over 1000 random realizations, *different* for each value of a . Panel c depicts the inhomogeneous broadening. It displays the fundamental cavity mode energy standard deviation $\sigma_\Omega = \langle (\Omega_0 - \langle \Omega_0 \rangle)^2 \rangle^{1/2}$ as a function of disorder parameter a . Panel d contains the same dependence as in panel b, but plotted instead as a function of a^2 .

The averaged position of the resonance does not shift significantly with the growth of the disorder parameter a . Fluctuations are due to the finite number of realizations used. The magnitude of the inhomogeneous broadening, which is given by σ_Ω , grows linearly with a , and the averaged half linewidth $\langle\Gamma_0\rangle$ grows quadratically with a (the latter is clearly visible in panel d). The inhomogeneous broadening matches the homogeneous linewidth of the resonance at $a \approx 0.02$.

The increase of the homogeneous linewidth results in a decrease of the averaged microcavity quality factor that depends quadratically on the disorder parameter a , as illustrated in Fig. 6.

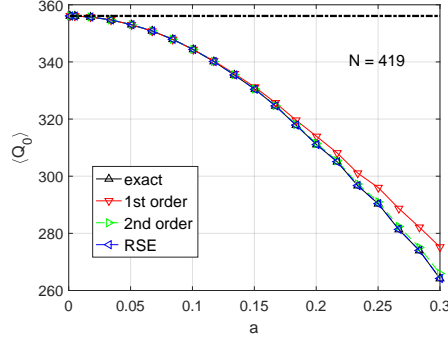


Fig. 6. (Color online) Dependence of the microcavity quality factor on the disorder parameter a , calculated exactly and in the first and second orders of perturbation theory, as well as by the resonant-state expansion with 419 states. The averaging is carried out over 1000 realizations of random displacements of inner interfaces in the microcavity.

5. Discussion

The reasons for the power scaling a^α of $\langle\Omega_0\rangle$, σ_Ω and $\langle\Delta\Gamma_0\rangle$ with $\alpha = 0, 1$ and 2 , respectively, can be understood in the first-order approximation of the resonant-state expansion.

The characteristic feature of the fundamental cavity mode electric field distribution for an unperturbed microcavity with exactly $\lambda/4$ Bragg pairs, exactly λ cavity layer, and with the boundary conditions of Eq. (13) can be clearly seen in Fig. 1. Namely, the values of the real and imaginary parts of the electric eigenfield are subsequently zeroed exactly at successive interfaces. As a result, in the vicinity of each interface, either the real or the imaginary part of the field is either a constant or a linear function of the distance to this interface $z - z_{0,j}$, i.e.,

$$\begin{aligned} \text{Re } \mathcal{E}_0^{(0)}(z) &\approx D_j + \mathcal{O}(z - z_{0,j}), \\ \text{Im } \mathcal{E}_0^{(0)}(z) &\approx (z - z_{0,j})F_j + \mathcal{O}\left((z - z_{0,j})^2\right), \end{aligned} \quad (20)$$

or

$$\begin{aligned} \text{Re } \mathcal{E}_0^{(0)}(z) &\approx (z - z_{0,j})D_j + \mathcal{O}\left((z - z_{0,j})^2\right), \\ \text{Im } \mathcal{E}_0^{(0)}(z) &\approx F_j + \mathcal{O}(z - z_{0,j}), \end{aligned} \quad (21)$$

where D_j, F_j are constants. The signs of D_j, F_j are identical (negative or positive) on the right-hand sides of the layers with larger dielectric susceptibility (i.e., for odd $j = 2m + 1$), and opposite on their left-hand sides (for even $j = 2m$). Note that $\Delta\varepsilon(z) = |\Delta\varepsilon|\text{sign}(z - z_{0,j})$ on such right-hand side interfaces, and $\Delta\varepsilon(z) = -|\Delta\varepsilon|\text{sign}(z - z_{0,j})$ on the left-hand side ones. Additionally, the normalization constant of the fundamental cavity mode is real, as discussed

in Appendix A. All this results in the following equation for the fundamental cavity mode eigenenergy, averaged over random realizations:

$$\langle E_0 \rangle = E_0 \left(1 - \frac{1}{2} \langle V_{00} \rangle \right) \equiv E_0 + \overline{\Delta E_0}, \quad (22)$$

with

$$\overline{\Delta E_0} = -\frac{E_0}{2} \sum_j \langle V_{00,j} \rangle, \quad (23)$$

where the sum is over all inner interfaces and

$$\begin{aligned} V_{00,j} &= C_0^{-2} \int_{z_{0,j}}^{z_{0,j}+a_j} \Delta \varepsilon(z) \mathcal{E}_0^2(z) dz \\ &\approx |\Delta \varepsilon| C_0^{-2} \begin{cases} \pm D_j^2 a_j^3 / 3 \mp F_j^2 a_j + i |D_j F_j| a_j^2, & j = 2m + 1 \\ \mp D_j^2 a_j \pm F_j^2 a_j^3 / 3 + i |D_j F_j| a_j^2, & j = 2m \end{cases} \end{aligned} \quad (24)$$

After averaging the odd powers of a_j vanish, and, as a result, we obtain in the first resonant-state expansion order and up to the second order in a

$$\langle \Delta \Omega_0 \rangle = 0, \quad \langle \Delta \Gamma_0 \rangle \propto a^2, \quad (25)$$

in agreement with the numerical results in Fig. 5a,b. As to the inhomogeneous broadening of Ω_0 , due to the terms linear in a_j , σ_Ω^2 is proportional to a^2 and thus $\sigma_\Omega \propto a$, in agreement with the numerical results in Fig. 5c.

This shows in particular the well known fact that the unperturbed planar Bragg microcavity is an *optimized* structure from the point of view of the maximum Q factor (or minimum of homogeneous half linewidth Γ_0): Any change of its structure causes a decrease of Q and increase of Γ_0 . In fact, in the case the unperturbed structure would not correspond to a minimum of Γ_0 versus layer thicknesses, a linear dependence of Γ_0 with a would be present.

6. Conclusion

To conclude, we have demonstrated that introducing random shifts of interfaces in a standard planar Bragg microcavity causes a growth of the inhomogeneous broadening of the fundamental cavity mode, linear in the disorder strength a , which quantifies the relative change of the layer thicknesses. In contrast, the linewidth increases proportionally to a^2 , with an according decrease of the quality factor. The inhomogeneous broadening starts to exceed the homogeneous one at a certain value of disorder parameter, which is $a \approx 0.02$ for the considered microcavity. The first-order perturbation theory within the resonant-state expansion works accurately up to a disorder strength of $a \approx 0.1$, especially for calculating the resonance energy. Furthermore, it allows to find a quantitative scaling of the microcavity parameters with disorder strength.

A. Appendix A: Poles of the scattering matrix via linearization

For normal incidence, the solutions of Maxwell equations for electric \mathbf{E} and magnetic \mathbf{H} fields in each layer of the microcavity

$$\mathbf{E} = (E_x, 0, 0), \quad \mathbf{H} = (0, H_y, 0), \quad (A1)$$

with

$$\begin{aligned} E_x &= A^+ \exp(-i\omega t + ik_l z) + A^- \exp(-i\omega t - ik_l z), \\ H_y &= n_l A^+ \exp(-i\omega t + ik_l z) - n_l A^- \exp(-i\omega t - ik_l z), \end{aligned} \quad (A2)$$

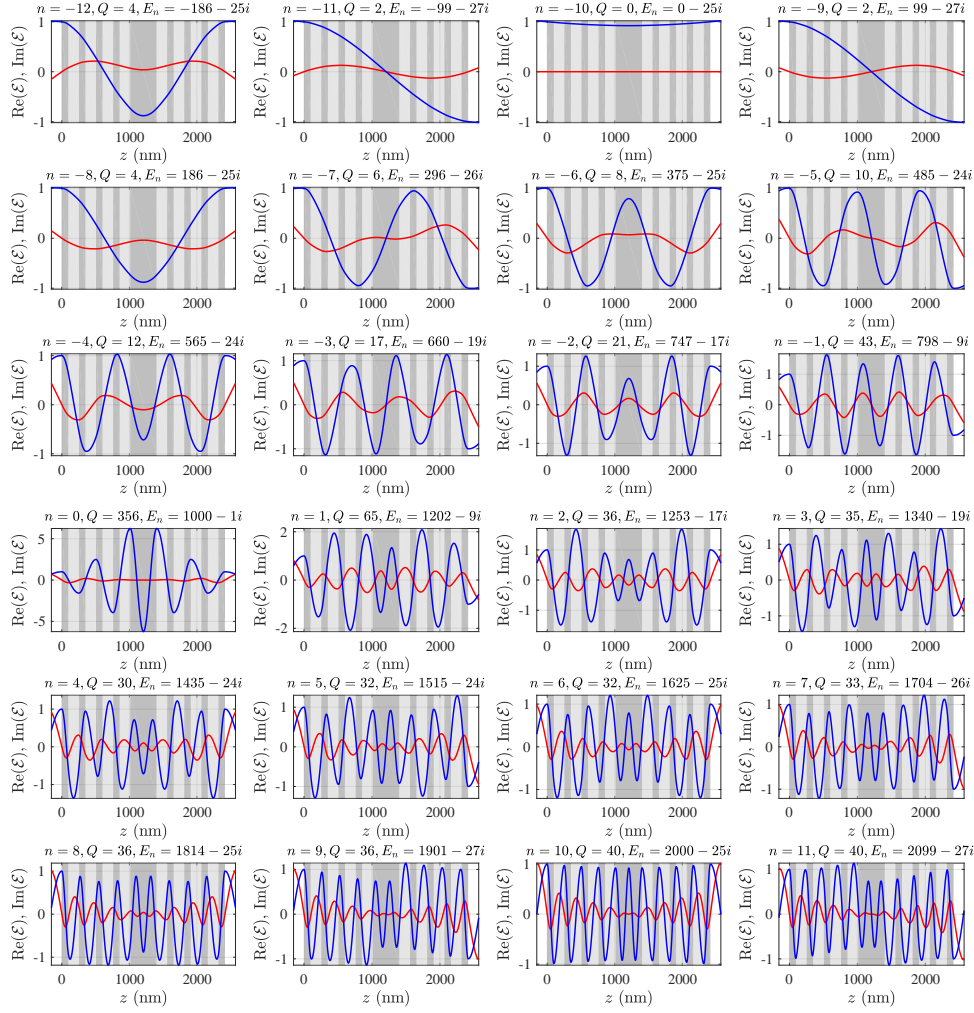


Fig. 7. (Color online) Real (blue solid lines) and imaginary (red solid lines) parts of the electric field distributions $\mathcal{E}_n^{(0)}(z)$ of the resonances of the ideal microcavity with $n = -12, -11, \dots, 11$, normalized according to conditions (13). The Q-factors and eigenenergies $E_n = \Omega_n - i\Gamma_n$ [in milli-electron volt (meV)] are shown in the title of each panel.

where $n_l = \sqrt{\varepsilon_l}$, $l = 0, 1, 2$, $\varepsilon_0 = 1$ corresponds to semi-infinite surrounding free space layers, and $k_l = n_l\omega/c$. Note that we are using the Gaussian units. Defining the amplitude vector as

$$|A\rangle = \begin{pmatrix} A^+ \\ A^- \end{pmatrix}, \quad (\text{A3})$$

the transfer matrix over a distance d inside a homogeneous and isotropic material is

$$\tilde{T}_{l,d} = \begin{pmatrix} \exp(ik_ld) & 0 \\ 0 & \exp(-ik_ld) \end{pmatrix}, \quad (\text{A4})$$

with $|A(z+d)\rangle = \tilde{T}_{l,d}|A(z)\rangle$. The transfer matrix over the interface from material l to l' is

$$T_{l',l} = \frac{1}{2} \begin{pmatrix} 1+K & 1-K \\ 1-K & 1+K \end{pmatrix}, \quad K = \frac{n_l}{n_{l'}}. \quad (\text{A5})$$

Table 1. The eigenenergies $E_n = \Omega_n - i\Gamma_n$ and normalization constants C_n^2 of 21 $-10 \leq n \leq 10$ resonances of the original ideal microcavity^a

n	Ω_n (meV)	Γ_n (meV)	$\text{Re}(C_n^2)$ (nm)	$\text{Im}(C_n^2)/\text{Re}(C_n^2)$
-10	0	24.8	$7.12 \cdot 10^3$	$3.15 \cdot 10^{-17}$
-9	99.2	26.5	$6.69 \cdot 10^3$	$3.17 \cdot 10^{-2}$
-8	186.3	25.0	$7.08 \cdot 10^3$	$6.54 \cdot 10^{-2}$
-7	295.6	25.7	$6.88 \cdot 10^3$	$9.99 \cdot 10^{-2}$
-6	375.3	25.0	$7.07 \cdot 10^3$	$1.39 \cdot 10^{-1}$
-5	485.3	23.7	$7.45 \cdot 10^3$	$1.84 \cdot 10^{-1}$
-4	565.4	23.6	$7.44 \cdot 10^3$	$2.39 \cdot 10^{-1}$
-3	659.5	19.1	$9.20 \cdot 10^3$	$2.98 \cdot 10^{-1}$
-2	746.6	17.3	$1.01 \cdot 10^4$	$3.72 \cdot 10^{-1}$
-1	797.9	9.18	$1.90 \cdot 10^4$	$4.28 \cdot 10^{-1}$
0	1000.0	1.40	$1.40 \cdot 10^5$	$1.17 \cdot 10^{-9}$
1	1202.0	9.18	$1.90 \cdot 10^4$	$-4.28 \cdot 10^{-1}$
2	1253.3	17.3	$1.01 \cdot 10^4$	$-3.72 \cdot 10^{-1}$
3	1340.4	19.1	$9.20 \cdot 10^3$	$-2.98 \cdot 10^{-1}$
4	1434.5	23.6	$7.44 \cdot 10^3$	$-2.39 \cdot 10^{-1}$
5	1514.6	23.7	$7.45 \cdot 10^3$	$-1.84 \cdot 10^{-1}$
6	1624.6	25.0	$7.07 \cdot 10^3$	$-1.39 \cdot 10^{-1}$
7	1704.3	25.7	$6.88 \cdot 10^3$	$-9.99 \cdot 10^{-2}$
8	1813.6	25.0	$7.08 \cdot 10^3$	$-6.54 \cdot 10^{-2}$
9	1900.7	26.5	$6.69 \cdot 10^3$	$-3.17 \cdot 10^{-2}$
10	2000.0	24.8	$7.12 \cdot 10^3$	$2.10 \cdot 10^{-8}$

^aThe parameters for the fundamental cavity mode with $n = 0$ are indicated by a frame.

We can calculate the transfer matrix over the entire microcavity as

$$T(\omega) = T_{0,1} \left(T_{BP}^{-1} \right)^4 \tilde{T}_{1,L_C} (T_{BP})^4 T_{1,0},$$

where

$$T_{BP} = T_{1,2} \tilde{T}_{2,L_2} T_{2,1} \tilde{T}_{1,L_1},$$

so that the amplitude vectors from the left and right sides of the microcavity are connected as

$$|A_L\rangle = \begin{pmatrix} A_L^+ \\ A_L^- \end{pmatrix}, \quad |A_R\rangle = \begin{pmatrix} A_R^+ \\ A_R^- \end{pmatrix}, \quad |A_L\rangle = T(\omega)|A_R\rangle. \quad (\text{A6})$$

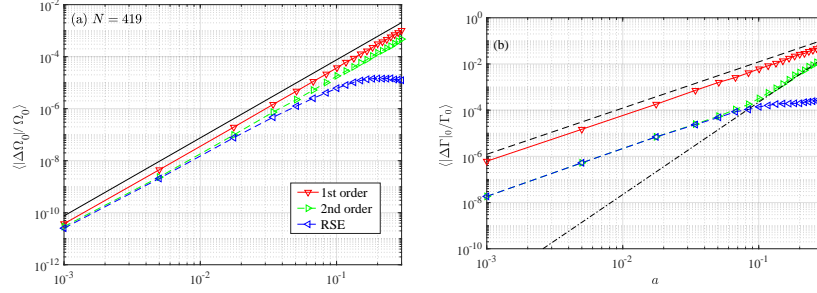


Fig. 8. (Color online) Relative accuracy of the first- and second-order perturbation theory, as well as the resonant-state expansion with 419 states for real (a) and imaginary (b) parts of the resonance energy as functions of disorder parameter a for the fundamental cavity mode, averaged over 1000 realizations of random interface displacements. Black dashed, solid, and dashed-dotted lines show a^2 , a^3 , and a^4 dependencies, respectively. The relative accuracy of the quality factor is same as shown in panel (b). The relative accuracy is calculated as the relative difference between the exact and the approximate methods.

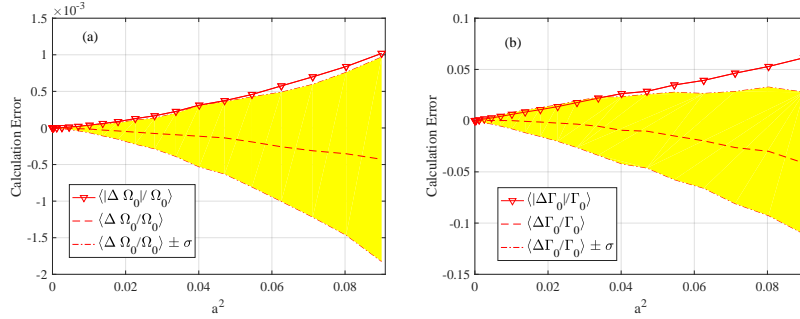


Fig. 9. (Color online) Relative calculation error of the first-order perturbation theory for real (a) and imaginary (b) parts of the resonance energy, as functions of a^2 for the fundamental cavity mode, averaged over 1000 realizations of random interface displacements. The dashed lines with open triangles are the same as shown in Fig. 8. The dashed red lines are averaged calculation errors $\langle \Delta \Omega_0 / \Omega_0 \rangle$ and $\langle \Delta \Gamma_0 / \Gamma_0 \rangle$. Yellow regions show the width of the error distribution, e. g., $\langle \Delta \Gamma_0 / \Gamma_0 \rangle \pm \sigma_\Delta$ in panel b.

Using the vectors of incoming and outgoing amplitudes

$$|\text{in}\rangle = \begin{pmatrix} A_L^+ \\ A_R^- \end{pmatrix}, \quad |\text{out}\rangle = \begin{pmatrix} A_L^- \\ A_R^+ \end{pmatrix} \quad (\text{A7})$$

the optical scattering matrix is defined as

$$|\text{out}\rangle = S(\omega)|\text{in}\rangle. \quad (\text{A8})$$

From this definition, it is seen that the physical meaning of the scattering matrix components is

$$S = \begin{pmatrix} r_{LL} & t_{RL} \\ t_{LR} & r_{RR} \end{pmatrix}, \quad (\text{A9})$$

where, e.g., r_{LL} is the amplitude reflection coefficient from the left side of microcavity to left, and t_{RL} is the amplitude transmission coefficient from left to right. The connection with the components of transfer matrix is

$$S = \begin{pmatrix} -T_{22}^{-1}T_{21} & T_{22}^{-1} \\ T_{11} - T_{12}T_{22}^{-1}T_{21} & T_{12}T_{22}^{-1} \end{pmatrix}, T = \begin{pmatrix} T_{11} & T_{12} \\ T_{21} & T_{22} \end{pmatrix}. \quad (\text{A10})$$

Eigensolutions (resonances) are found as nonvanishing outgoing solutions $|\text{out}\rangle = |o_n\rangle \neq 0$ at zero input $|\text{in}\rangle = 0$, which results in the homogeneous equation for the resonant outgoing eigenvectors $|o_n\rangle$ and eigenfrequencies ω_n :

$$S^{-1}(\omega_n)|o_n\rangle \equiv R(\omega_n)|o_n\rangle = 0. \quad (\text{A11})$$

Equation (A11) can be solved iteratively via a frequency-dependent linearization, described, e.g., in Ref. [18]. Assuming that

$$\omega_n = \omega + \Delta\omega,$$

and linearizing Eq. (A11) over $\Delta\omega$, we obtain

$$0 = R(\omega_n)|o_n\rangle = R(\omega)|o_n\rangle + \Delta\omega \frac{dR(\omega)}{d\omega}|o_n\rangle,$$

which requires

$$R(\omega)|o_n\rangle = -\Delta\omega \frac{dR(\omega)}{d\omega}|o_n\rangle.$$

Thus, we arrive at a linear 2×2 matrix problem to find $\Delta\omega$:

$$W|o_n\rangle = \Delta\omega|o_n\rangle, \quad (\text{A12})$$

where the matrix

$$W(\omega) \equiv - \left[\frac{dR(\omega)}{d\omega} \right]^{-1} R(\omega) = S(\omega) \left[\frac{dS(\omega)}{d\omega} \right]^{-1} \quad (\text{A13})$$

can be easily calculated and diagonalized. The latter equation follows from $d(SS^{-1})/d\omega = 0$. The minimum eigenvalue $\Delta\omega$ of W generates the corrected frequency $\omega' = \omega + \Delta\omega$, which is presumably closer to the solution of Eq. (A8). The procedure can be iteratively continued until finding the solution with the desired accuracy. As a starting point for iterations, it makes sense to use the real values of frequency, that correspond to the transmission maxima (see in Fig. 2).

As for the resonance eigenvector, it is known in the case of mirror-symmetric structure in advance due to symmetry constraints:

$$|o_n\rangle = \begin{pmatrix} 1 \\ (-1)^{p_n} \end{pmatrix}. \quad (\text{A14})$$

The parity is $p_n = 0$ for even and 1 for odd eigenfunctions. The resonance distribution of the electric field can be then reconstructed easily as

$$\mathcal{E}_n(z) = A_n^+(z) \exp(ik_n z) + A_n^-(z) \exp(-ik_n z), \quad (\text{A15})$$

with

$$\begin{pmatrix} A_n^+(z) \\ A_n^-(z) \end{pmatrix} = T_z(\omega_n) \begin{pmatrix} 0 \\ 1 \end{pmatrix}, \quad (\text{A16})$$

where $T_z(\omega_n)$ is the transfer matrix from the left side of the microcavity to point z inside.

The calculated eigenenergies and normalization constants for the 21 resonances around the resonance with $\Omega_0 = 1\text{eV}$ for our microcavity are given in Tab. 1. The resonance at $\Omega_0 = 1\text{eV}$ has the maximal quality factor. In the main text we call it the fundamental cavity mode. The electric eigenfields for $-12 \leq n \leq 11$ are shown in Fig. 7. The resonance with $n = -10$ is ‘static’, $\Omega_{-10} = 0$. All other resonances are mirror-symmetric on the complex energy plane around it: the resonances with $\tilde{n} = n + 10 < 0$ are $\Omega_{\tilde{n}-10} = -\Omega_{-\tilde{n}-10} < 0$, $\Gamma_{\tilde{n}-10} = \Gamma_{-\tilde{n}-10}$, and the eigenfields are complex conjugate, i.e., $\text{Re } \mathcal{E}_{\tilde{n}-10}(z) = \text{Re } \mathcal{E}_{-\tilde{n}-10}(z)$, $\text{Im } \mathcal{E}_{\tilde{n}-10}(z) = -\text{Im } \mathcal{E}_{-\tilde{n}-10}(z)$. The parity of the resonance with odd (even) n is odd (even). The latter is the consequence of the mirror symmetry of the microcavity and the definition of normalized resonant states using the boundary conditions Eq. A14. Note that the normalization constants C_n are, generally, complex (except those of the fundamental cavity mode and other high-Q states, see below). We use in the main text up to $N = 419$ states in the resonant-state expansion basis, positioned symmetrically around the fundamental cavity mode, i.e., with Ω_n for $-(N-1)/2 \leq n \leq (N-1)/2$.

An interesting point about the normalization constant of the fundamental cavity mode is that it appears to be real within the accuracy of our numerical calculation. In fact,

$$C_{0,1} = \int_0^L \varepsilon(x) \mathcal{E}_0^2(x) dx \approx 1.4004 \cdot 10^5 - 1.9733 \cdot 10^2 i$$

and

$$C_{0,2} = \frac{i}{2k_0} [\mathcal{E}_0^2(0) + \mathcal{E}_0^2(L)] \approx -2.7708 \cdot 10^{-1} + 1.9733 \cdot 10^2 i$$

for the eigenfield \mathcal{E}_0 , shown in Fig. 1. This field is normalized according to

$$\mathcal{E}_0^{(0)}(0) = \mathcal{E}_0^{(0)}(L) = 1,$$

which follows from Eq. (A14). It appears that for the fundamental cavity mode with $n = 0$

$$C_0^2 = C_{0,1} + C_{0,2} \approx 1.4004 \cdot 10^5 + 1.6502 \cdot 10^{-4} i,$$

so that C_0 is real with the accuracy of our numerical procedure.

B. Appendix B: Accuracy of different approximations of the resonant-state expansion

The averaged absolute values of relative errors for calculating Ω_0 and Γ_0 by the first- and second-order approximations and the resonant-state expansion with 419 nearest resonant states are illustrated in Fig. 8 (panels a and b, respectively) as functions of the disorder parameter a . It can be seen that the first-order perturbation theory becomes, as expected, less accurate with increasing disorder parameter, but it gives in most cases quite accurate results, especially for the calculation of Ω_0 , and for small amplitude of disorder, $a < 0.1$.

Figure 8a contains also, as a guide for the eye, black solid line, proportional to a^3 , and Fig. 8b contains black dashed and dashed-dotted ones, proportional to a^2 and a^4 , respectively. The magnitude of the calculation errors grows as a^3 and a^2 for the first perturbation order over the investigated range of a for Ω_0 and Γ_0 , respectively. For Ω_0 , the second order only provides a factor of 2 improvement and is limited by the basis size used in the resonant-state expansion. The calculation error in the second perturbation order scales instead as a^4 for Γ_0 , but is limited for

small a by the finite size of the resonant-state expansion basis used and merges with the error of the full resonant-state expansion. As to the calculation error of the full resonant-state expansion, in the case of Γ_0 it saturates around 2×10^{-4} for $a > 0.1$. For $a \lesssim 0.02$ the full resonant-state expansion error coincides with that of the second order perturbation theory which means that the full resonant-state expansion becomes redundant. However, the value of a where the second order matches the full resonant-state expansion depends on the basis size. The saturated accuracy of the full resonant-state expansion for larger a depends on the chosen basis size. With decrease of the size of the resonant state basis this saturated accuracy worsens, e.g., to $\sim 2 \times 10^{-3}$ for $N = 219$. Note that we take here the resonant state basis set symmetrical around the fundamental cavity mode.

As a result, the first-order perturbation theory of resonant-state expansion works well for $a < 0.3$. Note that such a large a corresponds to the amplitude of interface displacement of up to 30% of the thinner Bragg layer thickness, or in the present case as large as ~ 30 nm. The averaged calculation error of the first-order perturbation is still smaller than 10% for $a = 0.3$. Of course, as can be understood from Fig. 2 and Fig. 3, there occur relatively rare displacement realizations with a very large calculation error. However, the majority of disorder realizations is still reasonably well described by first-order perturbation theory. Figure 9 illustrates the width of the range within which more than half of the disorder realizations are confined (filled by yellow color). With growing disorder parameter systematic errors arise $\langle \Delta\Omega_0/\Omega_0 \rangle < 0$ and $\langle \Delta\Gamma_0/\Gamma_0 \rangle < 0$. However, for weak disorder these systematic errors are small, and $\langle |\Delta\Omega_0|/\Omega_0 \rangle \approx \sigma_{\Delta\Omega/\Omega}$, $\langle |\Delta\Gamma_0|/\Gamma_0 \rangle \approx \sigma_{\Delta\Gamma/\Gamma}$.

Funding

Deutsche Forschungsgemeinschaft (Mercator-Fellowship, SPP 1839); Russian Science Foundation (16-12-10538II).

Acknowledgments

The authors acknowledge support from DFG, and Russian Academy of Sciences. S.G.T. and N.A.G. thank the Russian Science Foundation (Grant No. 16-12-10538II) for support in part of the calculations of the exact microcavity resonant states.

Disclosures

The authors declare no conflicts of interest.

References

1. P. Vukusic and J. R. Sambles, "Photonic structures in biology," *Nature* **424**, 852–855 (2003).
2. H. Zi, X. D. Yu, Y. Z. Li, X. H. Hu, C. Xu, X. J. Wang, X. H. Liu, and R. T. Fu, "Coloration strategies in peacock feathers," *Proc. Nat. Acad. Sci. USA* **100**, 12576–12578 (2003).
3. S. Kinoshita, S. Yoshioka, and J. Miyazaki, "Physics of structural colors," *Reports on Prog. Phys.* **71**, 076401 (2008).
4. D. S. Wiersma, "Disordered photonics," *Nat. Photonics* **7**, 188–196 (2013).
5. X. Wu, F. L. Rodríguez-Gallegos, M.-C. Heep, B. Schwind, G. Li, H.-O. Fabritius, G. von Freymann, and J. Förstner, "Polarization conversion effect in biological and synthetic photonic diamond structures," *Adv. Opt. Mater.* **6**, 1800635 (2018).
6. D. Gerace and L. C. Andreani, "Effects of disorder on propagation losses and cavity q-factors in photonic crystal slabs," *Photonics Nanostructures - Fundamentals Appl.* **3**, 120–128 (2005). The Sixth International Symposium on Photonic and Electromagnetic Crystal Structures (PECS-VI).
7. Y. Taguchi, Y. Takahashi, Y. Sato, T. Asano, and S. Noda, "Statistical studies of photonic heterostructure nanocavities with an average q factor of three million," *Opt. Express* **19**, 11916–11921 (2011).
8. K. Ashida, M. Okano, T. Yasuda, M. Ohtsuka, M. Seki, N. Yokoyama, K. Koshino, K. Yamada, and Y. Takahashi, "Photonic crystal nanocavities with an average q factor of 1.9 million fabricated on a 300-mm-wide soi wafer using a cmos-compatible process," *J. Light. Technol.* **36**, 4774–4782 (2018).

9. M. S. Mohamed, Y. Lai, M. Minkov, V. Savona, A. Badolato, and R. Houdré, "Influence of disorder and finite-size effects on slow light transport in extended photonic crystal coupled-cavity waveguides," *ACS Photonics* **5**, 4846–4853 (2018).
10. G. Demésy, F. Zolla, A. Nicolet, M. Commandré, and C. Fossati, "The finite element method as applied to the diffraction by an anisotropic grating," *Opt. Express* **15**, 18089–18102 (2007).
11. H. Hagino, Y. Takahashi, Y. Tanaka, T. Asano, and S. Noda, "Effects of fluctuation in air hole radii and positions on optical characteristics in photonic crystal heterostructure nanocavities," *Phys. Rev. B* **79**, 085112 (2009).
12. S. G. Johnson, M. Ibanescu, M. A. Skorobogatiy, O. Weisberg, J. D. Joannopoulos, and Y. Fink, "Perturbation theory for maxwell's equations with shifting material boundaries," *Phys. Rev. E* **65**, 066611 (2002).
13. J. Wiersig and J. Kullig, "Optical microdisk cavities with rough sidewalls: A perturbative approach based on weak boundary deformations," *Phys. Rev. A* **95**, 053815 (2017).
14. J. P. Vasco and V. Savona, "Disorder effects on the coupling strength of coupled photonic crystal slab cavities," *New J. Phys.* **20**, 075002 (2018).
15. J. P. Vasco and S. Hughes, "Anderson localization in disordered photonic crystal slab cavities," *ACS Photonics* **5**, 1262–1272 (2018).
16. P. T. Leung, S. Y. Liu, and K. Young, "Completeness and orthogonality of quasinormal modes in leaky optical cavities," *Phys. Rev. A* **49**, 3057–3067 (1994).
17. S. G. Tikhodeev, A. L. Yablonskii, E. A. Muljarov, N. A. Gippius, and T. Ishihara, "Quasiguidded modes and optical properties of photonic crystal slabs," *Phys. Rev. B* **66**, 045102 (2002).
18. N. A. Gippius, S. G. Tikhodeev, and T. Ishihara, "Optical properties of photonic crystal slabs with an asymmetrical unit cell," *Phys. Rev. B* **72**, 045138 (2005).
19. E. A. Muljarov, W. Langbein, and R. Zimmermann, "Brillouin-wigner perturbation theory in open electromagnetic systems," *EPL* **92**, 50010 (2010).
20. M. B. Doost, W. Langbein, and E. A. Muljarov, "Resonant-state expansion applied to planar open optical systems," *Phys. Rev. A* **85**, 023835 (2012).
21. E. A. Muljarov and W. Langbein, "Exact mode volume and purcell factor of open optical systems," *Phys. Rev. B* **94**, 235438 (2016).
22. F. Alpeggiani, N. Parappurath, E. Verhagen, and L. Kuipers, "Quasinormal-mode expansion of the scattering matrix," *Phys. Rev. X* **7**, 021035 (2017).
23. E. Lassalle, N. Bonod, T. Durt, and B. Stout, "Interplay between spontaneous decay rates and lamb shifts in open photonic systems," *Opt. Lett.* **43**, 1950–1953 (2018).
24. W. Yan, R. Faggiani, and P. Lalanne, "Rigorous modal analysis of plasmonic nanoresonators," *Phys. Rev. B* **97**, 205422 (2018).
25. P. Lalanne, W. Yan, K. Vynck, C. Sauvan, and J.-P. Hugonin, "Light interaction with photonic and plasmonic resonances," *Las. & Phot. Rev.* **12**, 1700113 (2018).
26. P. Lalanne, W. Yan, A. Gras, C. Sauvan, J.-P. Hugonin, M. Besbes, G. Demésy, M. D. Truong, B. Gralak, F. Zolla, A. Nicolet, F. Binkowski, L. Zschiedrich, S. Burger, J. Zimmerling, R. Remis, P. Urbach, H. T. Liu, and T. Weiss, "Quasinormal mode solvers for resonators with dispersive materials," *J. Opt. Soc. Am. A* **36**, 686–704 (2019).
27. J. Defrance and T. Weiss, "On the pole expansion of electromagnetic fields," *Opt. Express* **28**, 32363–32376 (2020).
28. U. Fano, "The theory of anomalous diffraction gratings and of quasi-stationary waves on metallic surfaces (sommerfeld's waves)," *J. Opt. Soc. Am.* **31**, 213–222 (1941).
29. U. Fano, "Effects of configuration interaction on intensities and phase shifts," *Phys. Rev.* **124**, 1866–1878 (1961).
30. B. Luk'yanchuk, N. I. Zheludev, S. A. Maier, N. J. Halas, P. Nordlander, H. Giessen, and C. T. Chong, "The fano resonance in plasmonic nanostructures and metamaterials," *Nat Mater* **9**, 707–715 (2010).
31. E. A. Muljarov and W. Langbein, "Resonant-state expansion of dispersive open optical systems: Creating gold from sand," *Phys. Rev. B* **93**, 075417 (2016).
32. S. Neale and E. A. Muljarov, "Resonant-state expansion for planar photonic crystal structures," *Phys. Rev. B* **101**, 155128 (2020).
33. T. Weiss, M. Mesch, M. Schäferling, H. Giessen, W. Langbein, and E. A. Muljarov, "From dark to bright: first-order perturbation theory with analytical mode normalization for plasmonic nanoantenna arrays applied to refractive index sensing," *Phys. Rev. Lett.* **116**, 237401 (2016).
34. T. Weiss, M. Schäferling, H. Giessen, N. A. Gippius, S. G. Tikhodeev, W. Langbein, and E. A. Muljarov, "Analytical normalization of resonant states in photonic crystal slabs and periodic arrays of nanoantennas at oblique incidence," *Phys. Rev. B* **96**, 045129 (2017).
35. E. A. Muljarov and T. Weiss, "Resonant-state expansion for open optical systems: generalization to magnetic, chiral, and bi-anisotropic materials," *Opt. Lett.* **43**, 1978–1981 (2018).
36. L. J. Armitage, M. B. Doost, W. Langbein, and E. A. Muljarov, "Resonant-state expansion applied to planar waveguides," *Phys. Rev. A* **89**, 053832 (2014).
37. L. J. Armitage, M. B. Doost, W. Langbein, and E. A. Muljarov, "Erratum: Resonant-state expansion applied to planar waveguides [phys. rev. a 89, 053832 (2014)]," *Phys. Rev. A* **97**, 049901 (2018).
38. S. Uppend, I. Allayarov, M. A. Schmidt, and T. Weiss, "Analytical mode normalization and resonant state expansion for bound and leaky modes in optical fibers - an efficient tool to model transverse disorder," *Opt. Express* **26**, 22536–22546 (2018).

39. S. V. Lobanov, G. Zorinians, W. Langbein, and E. A. Muljarov, "Resonant-state expansion of light propagation in nonuniform waveguides," *Phys. Rev. A* **95**, 053848 (2017).
40. I. Allayarov, S. Upendar, M. A. Schmidt, and T. Weiss, "Analytic mode normalization for the kerr nonlinearity parameter: Prediction of nonlinear gain for leaky modes," *Phys. Rev. Lett.* **121**, 213905 (2018).
41. I. Allayarov, M. A. Schmidt, and T. Weiss, "Theory of four-wave mixing for bound and leaky modes," *Phys. Rev. A* **101**, 043806 (2020).
42. S. Both and T. Weiss, "First-order perturbation theory for changes in the surrounding of open optical resonators," *Opt. Lett.* **44**, 5917–5920 (2019).
43. N. A. Gippius, T. Weiss, S. G. Tikhodeev, and H. Giessen, "Resonant mode coupling of optical resonances in stacked nanostructures," *Opt. Express* **18**, 7569–7574 (2010).
44. T. Weiss, N. A. Gippius, S. G. Tikhodeev, G. Granet, and H. Giessen, "Derivation of plasmonic resonances in the fourier modal method with adaptive spatial resolution and matched coordinates," *J. Opt. Soc. Am. A* **28**, 238–244 (2011).
45. J. M. Zajac and W. Langbein, "Structure and zero-dimensional polariton spectrum of natural defects in gaas/alas microcavities," *Phys. Rev. B* **86**, 195401 (2012).
46. M. B. Doost, W. Langbein, and E. A. Muljarov, "Resonant-state expansion applied to three-dimensional open optical systems," *Phys. Rev. A* **90**, 013834 (2014).
47. G. Christmann, D. Simeonov, R. Butté, E. Feltn, J.-F. Carlin, and N. Grandjean, "Impact of disorder on high quality factor iii-v nitride microcavities," *Appl. Phys. Lett.* **89**, 261101 (2006).
48. v. Gačević, G. Rossbach, R. Butté, F. Réveret, M. Glauser, J. Levrat, G. Cosendey, J.-F. Carlin, N. Grandjean, and E. Calleja, "Q-factor of (in,ga)n containing iii-nitride microcavity grown by multiple deposition techniques," *J. Appl. Phys.* **114**, 233102 (2013).
49. v. Gačević and N. Vukmirović, "Effective refractive-index approximation: A link between structural and optical disorder of planar resonant optical structures," *Phys. Rev. Appl.* **9**, 064041 (2018).
50. P. Billingsley, *Probability and Measure, Third Edition* (John Wiley & Sons, Inc., 1995), Sec. 27.
51. W. Voigt, "Über das Gesetz der Intensitätsverteilung innerhalb der Linien eines Gasspektrums," *Sitzungsber. K. B. Akad. Wiss. München, math.-phys. Kl.* pp. 603–620 (1912).
52. F. W. J. Olver, D. W. Lozier, R. F. Boisvert, and C. W. Clark, eds., *NIST Handbook of Mathematical Functions Hardback and CD-ROM* (Cambridge University Press, 2010), chap. 7.19.